Cronfa - Swansea University Open Access Repository

Enhanced thermoelectric performance of monolayer MoSSe, bilayer MoSSe and graphene/MoSSe heterogeneous nanoribbons

Shuo Deng[†‡] Lijie Li[*‡], Owen J. Guy[*‡], and Yan Zhang[*§]

[†]Wuhan University of Technology, Wuhan 430070, China

[‡]College of Engineering, Swansea University, Swansea SA1 8EN, UK

[§]School of Physics, University of Electronic Science and Technology of China, Chengdu, China.

[*]Emails: L.Li@swansea.ac.uk; o.j.guy@swansea.ac.uk; zhangyan@uestc.edu.cn

Abstract:

Graphene has many superlative thermal, electrical and mechanical properties. However, the thermoelectric performance of graphene is limited by its high thermal conductivity and small Seebeck coefficient. To address this problem, monolayer and bilayer MoSSe nanoribbons together with the graphene/MoSSe heterostructures have been investigated in this work. Electron and phonon transport, and the thermoelectric properties of the monolayer and bilayer MoSSe nanoribbons, together with the graphene/MoSSe heterostructures have been analyzed by first-principle methods in conjunction with non-equilibrium Green's function and Landauer equation. Results indicate that figure of merit (*ZT)* values of 2.01 and 1.64 can be achieved for the graphene/SeMoS stacked nanoribbon and symmetric armchair MoSSe nanoribbon respectively at 300 K, which are much higher than the *ZT* value of prime graphene (*ZT*~0.05) [1]. The maximum *ZT* values of these structures increase at T<350 K, while the maximum *ZT* decreases at high temperatures (T>350 K). However, the maximum *ZT* values of the symmetric armchair MoSSe nanoribbon show an increase with temperatures up to 550 K. From our analysis, phonon thermal conductivity and temperature are key factors determining the *ZT* values in MoSSe nanoribbons. The significantly enhanced *ZT* values make graphene/SeMoS stacking nanoribbons and symmetric armchair MoSSe nanoribbons promising candidate devices for thermoelectric applications.

Keywords: thermoelectric, MoSSe, graphene/MoSSe, first principles method

Introduction:

Since 2009 there has been a surge of research interest in reducing the demand for fossil fuels by developing renewable energy resources. Among many energy conversion techniques, thermoelectric conversion offers a green option for harvesting electrical power from waste heat [2-4]. The energy conversion efficiency of a thermoelectric device is characterized by the figure of merit $ZT = S^2 G_e T / \left(k_e + k_{ph} \right)$, where the *S, Ge* and *T* are the Seebeck coefficient, electrical conductivity and temperature, respectively and k_e and k_{ph} are the thermal conductivity of electrons and phonons, respectively. A good thermoelectric device should have low thermal conductivity, high electrical conductivity and a high Seebeck coefficient. However, according to the Wiedemann-Franz law and Mott formula, increasing electrical conductivity usually leads to enhancement in the thermal conductivity of electrons, hence reducing the Seebeck

coefficient, which means that it is very difficult to control the thermal conductivity, electrical conductivity and Seebeck coefficient, independently [5]. As a result, the key to improving the thermoelectric performance of a device is to find a trade-off between the Seebeck coefficient, electrical conductivity and thermal conductivity.

In the prior research, a relatively high in-plane Hall mobility (over 34000 cm^2 V^{-1} s^{-1})[6], wide tunable range of Seebeck coefficient (-4×10^2 ~ -1×10^5 μV K^{-1})[7], and relatively low thermal conductivity (62.2 W m^{-1} K^{-1})[8] of monolayer MoS_2 were demonstrated, which indicates transition metal dichalcogenides (TMDs) are particularly suited for thermoelectric applications [9-12]. In 2017, the first true Janus TMD was discovered- MoSSe, which was fabricated by fully replacing one S atoms with Se atoms within the monolayer MoS_2 using the chemical vapour deposition (CVD)[13]. Compared with traditional TMDs materials, monolayer MoSSe has greater stability in its out-of-plane structure asymmetry, which yields a large intrinsic dipole[14, 15], spin-orbit coupling dependent band structures[13] and piezoelectricity properties[13, 16]. Although there has been some theoretical and experimental work reported on the relevant applications for the monolayer MoSSe including the natural doping[17, 18], solar water splitting[19-21], optoelectronic devices[22, 23], and bandgap engineering[24], the thermoelectric performance of MoSSe nanostructures has not been fully explored. The experiments demonstrating synthesis of MoSSe monolayer and TMDs/Graphene heterostructures have been reported in some prior papers[13, 14, 25]. MoSSe nanostructures have shown great potential in the thermoelectric devices but have not been explored in experiment. Therefore, it is imperative to conduct some theoretical work, which can serve as design guides for further experimentation.

In this work, the electron, phonon transport and thermoelectric performance of monolayer MoSSe nanoribbons, bilayer MoSSe nanoribbons and graphene/MoSSe heterostructure nanoribbons are systematically researched using first-principles calculations with non-equilibrium Green's function and Landauer equation, which has been applied in previous studies on TMDs thermoelectric performance[26-30]. It is discovered that the phonon contribution to the overall thermal conductivity is much more important than the electron conductivity in these MoSSe nanostructures. Moreover, *ZT* values of 2.01 and 1.64 can be achieved for the graphene/SeMoS stacked nanoribbons and symmetric armchair MoSSe nanoribbons at 300 K.

Computation Procedure:
In the present model, *ab initio* simulations are performed using density functional theory (DFT) implemented in the Atomistix ToolKit (ATK2018) simulation tools[31]. The exchange-correlation functional chooses the generalized gradient approximation (GGA) with the parametrization of Perdew-Burke-Ernzerhof (PBE) used in the structure optimization. In the bilayer MoSSe nanostructures, in order to consider the van der Waals (vdW) interaction between two layers, we used semi-empirical corrections in the Grimme DFT-D2 model[32]. In the optimization simulation, the cutoff energy of 150 Ry and 15×15×1 k-points grid were used in the Brillouin zone. The structure is fully relaxed until the force on each atom becomes smaller than 0.01 eV/Å, and the stress error tolerance is 0.001 eV/ $Å^3$. In our electron and phonon transport calculation, a vacuum spacing of at least 20 Å in the normal direction to the electron transport plane was used to avoid interactions of the periodic boundary conditions.

The Brillouin zone of the MoSSe nanoribbon device is sampled by a $1\times1\times200$ k-mesh and a double-zeta polarized for all atoms. In the transport regime, the electrical conductivity, Seebeck coefficient and electronic thermal conductivity are calculated using the first-principles calculations with the non-equilibrium Green's function. The phonon thermal conductivity is calculated based on the Landauer equation. First, the electron (T_e) and phonon (T_p) transmission function are deduced from the Green's functions of the electron Schrodinger equation and lattice dynamic equation, respectively. Then, the current across the MoSSe nanoribbon device can be calculated as:

$$I = \frac{e}{h}\int_{\mu_L}^{\mu_R}\left(f_L(\text{E}) - f_R(\text{E})\right)T_e(E)dE \qquad (1)$$

where, h is the Planck's constant, μ_L and μ_R are the chemical potentials of left and right electrodes, $f_L(E)$ and $f_R(E)$ are the Fermi distribution functions of the left and right electrode. The electrical conductivity (G_e) is calculated from a function of the Fermi energy μ as:

$$G_e(\mu) = \frac{2e}{h}T_e(\mu) \qquad (2)$$

The Seebeck coefficient and electronic thermal conductivity can be calculated from the intermediate function L_n:

$$L_n(\mu,T) = \frac{2}{h}\int T_e(E)(E-\mu)^n \frac{-\partial f(E,\mu,\text{T})}{\partial E}dE \qquad (3)$$

where f is the Fermi distribution function at the temperature T. In the end, the Seebeck coefficient (S) and electronic thermal conductivity (K_e) can be calculated as:

$$S(\mu,\text{T}) = \frac{1}{eT}\frac{L_1(\mu,\text{T})}{L_0(\mu,\text{T})} \qquad (4)$$

$$K_e(\mu,\text{T}) = \frac{1}{T}\left[L_2(\mu,\text{T}) - \frac{L_1(\mu,T)^2}{L_0(\mu,T)^2}\right] \qquad (5)$$

The phonon thermal conductivity (K_p) is calculated from the Landauer equation:

$$K_p = \int T_p(\omega)\left[\frac{\partial n(\omega,T)}{\partial T}\right]\frac{\hbar\omega}{2\pi}d\omega \qquad (6)$$

where $n(\omega,T)$ is the Bose-Einstein distribution function at the temperature T, ω is the phonon frequency and $\hbar$ is the reduced Planck's constant. The phonon thermal conductivity can be rewritten in a temperature depend form:

$$K_p(T) = \frac{1}{8\pi k_B T^2}\int_0^\infty \hbar^2\omega^2 \frac{T_p(\omega)}{\sinh^2(\hbar\omega/2k_BT)}d\omega \qquad (7)$$

where k_B is the Boltzmann constant.

Results and Discussions:

As shown in Figure 1, to construct the models of MoSSe nanoribbons, we firstly optimized the lattice parameters of the monolayer MoSSe. For the monolayer MoSSe, the optimized lattice parameters are a=b=3.22 Å. The distance between S and Se atom is 3.23 Å and the angle between the Mo-S and Mo-Se bonds is 81.4°, which is consistent with previously reported experimental results[13]. Because the GGA-PBE method usually underestimates the bandgap, we used the Heyd-Scuseria-Ernzerhof (HSE) method in our band structure simulations. The HSE bandgap of the monolayer MoSSe are 2.04 eV, which corresponds well with the 1.77 eV optical bandgap from experimental measurement [13]. Figure 1c shows the band structures of the Brillouin zone of high symmetry points along the path through Γ-M-K-Γ and the projected density of state (PDOS) of the monolayer MoSSe. Calculation results show that monolayer MoSSe displays a direct bandgap with the conduction band minimum (CBM) and valence band maximum (VBM) located at the K point in the Brillouin zone. Moreover, as shown in Figure 1d, the PDOS of CBM and VBM of the monolayer MoSSe are contributed mainly from the Mo-d orbital. Moreover, we calculated a 3.71 eV electron affinity of the monolayer MoSSe.
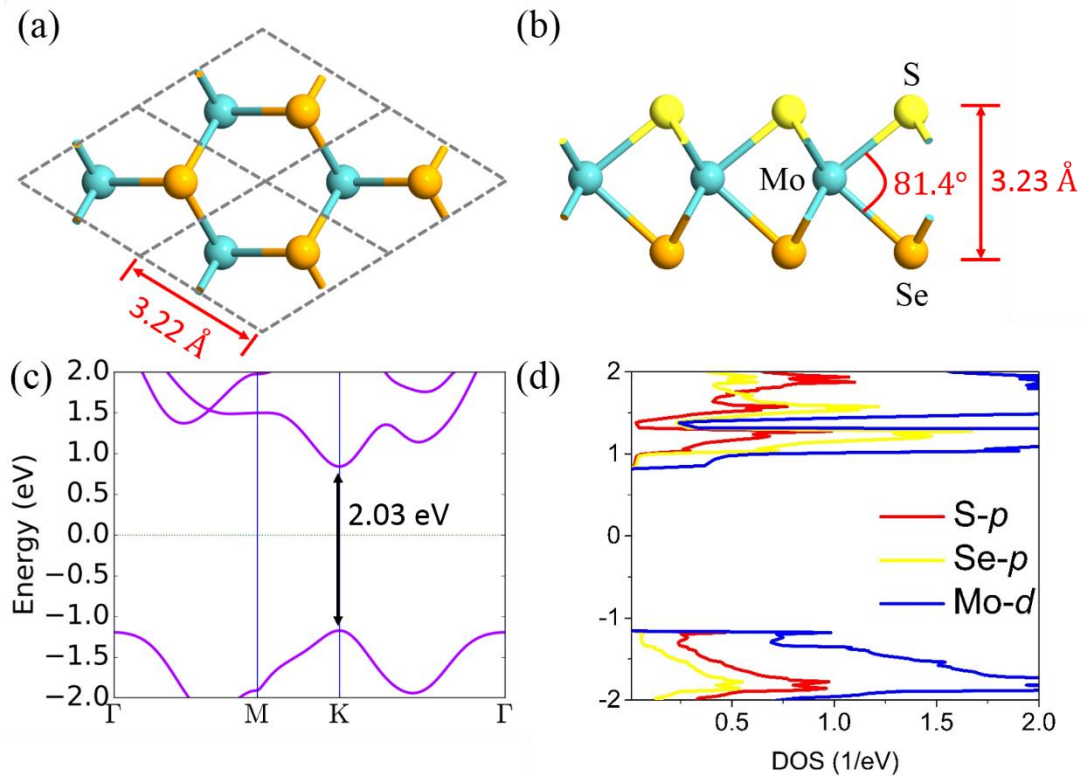

Figure 1. Geometric structure (a)-(b), band structure (c) and projected density of state (d) of monolayer MoSSe.

Figure 2 shows the relaxed structures and band structures of monolayer MoSSe nanoribbons, which can be obtained by cutting the monolayer MoSSe. Depending on the edge shape of nanoribbons, we classify them into armchair MoSSe nanoribbons and zigzag MoSSe nanoribbons. Moreover, based on the edge symmetries of armchair MoSSe nanoribbons, they can be constructed as: symmetric armchair MoSSe nanoribbons (ac-s) and asymmetric armchair MoSSe nanoribbons (ac-u). Similarly, zigzag MoSSe nanoribbons can be constructed as symmetric zigzag MoSSe nanoribbons (zz-s) and asymmetric zigzag MoSSe nanoribbons (zz-u). In order to improve the stabilities of the nanoribbons, we induce the hydrogen-

passivated at the edge of MoSSe nanoribbons in our transport simulation. As shown in Figures 2a and 2b, the calculated band structures of the ac-s and ac-u show that they are direct bandgap semiconductors with bandgap of 0.29 eV and 0.12 eV, respectively, while Figures 2c and 2d show that zigzag MoSSe nanoribbons are metallic. These electronic properties of MoSSe nanoribbon are similar to the MoS_2 nanoribbons[33]. Those various band structures indicate different electronic conductivities and Seebeck coefficients, which influence thermoelectric performance of these MoSSe-based nanoribbons. From the reference[34], it is seen that the bandgap of MoSSe nanotube is about 1.44 eV, which is far larger than the symmetric armchair MoSSe nanoribbon (0.29 eV). Moreover, the different band structures will induce different electronic conductivities of MoSSe nanotube and nanoribbon.
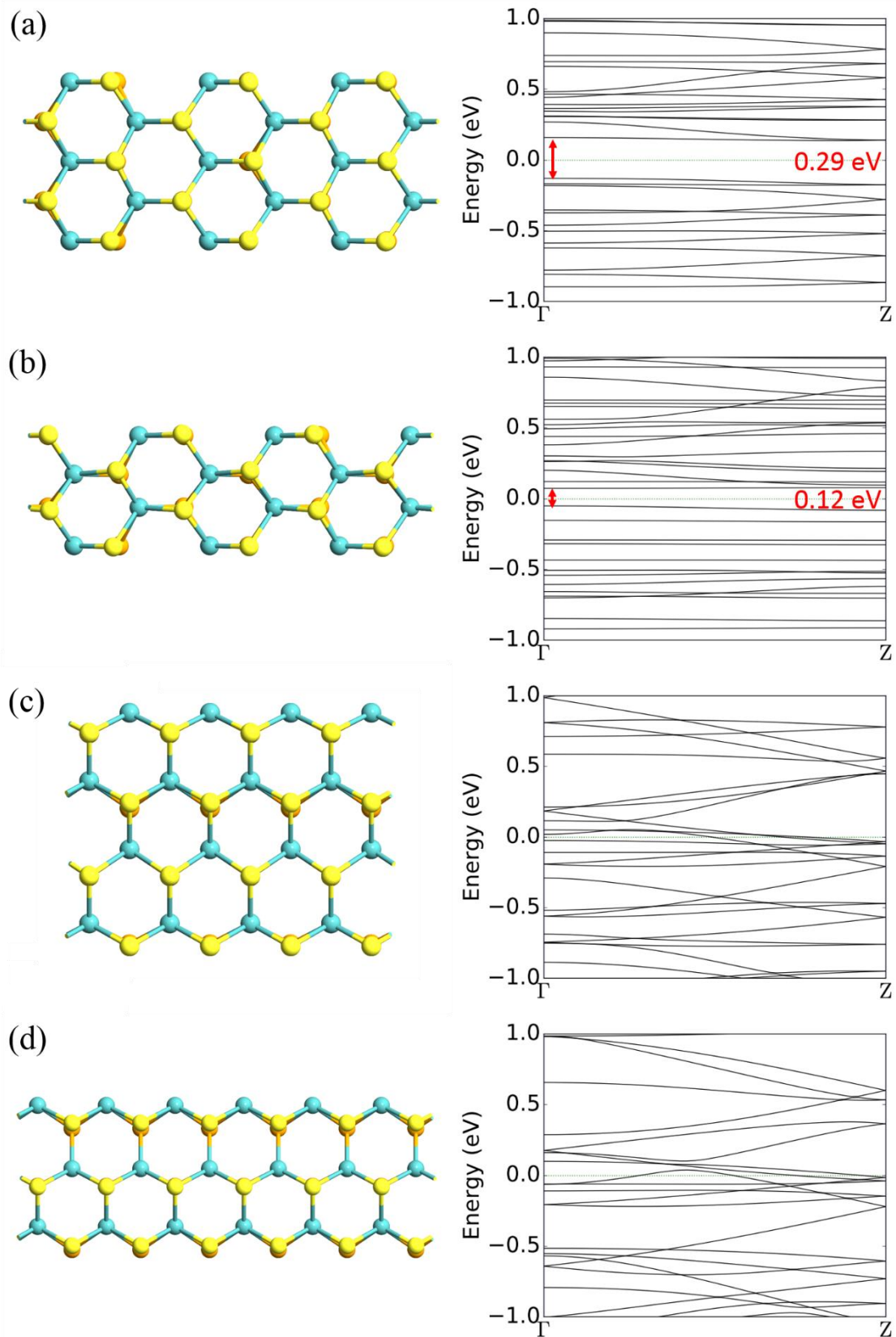
Figure 2. Relaxed structure and band structure of symmetric armchair MoSSe nanoribbon (ac-s) (a), asymmetric armchair MoSSe nanoribbon (ac-u) (b), symmetric zigzag MoSSe nanoribbon (zz-s) (c) and asymmetric zigzag MoSSe nanoribbon (zz-u) (d).

The electron and phonon transmission spectra of MoSSe nanoribbons are given in (Figures 3a and 3b) indicate that electron and phonon transmission values of zigzag MoSSe nanoribbons are far higher than the armchair MoSSe nanoribbons, which is consistent with the band analysis results that zigzag MoSSe nanoribbons are metallic while armchair MoSSe nanoribbons are semiconducting. Figures 3c and 3d show the calculated *I-V* and *dI/dV* curves for armchair and zigzag MoSSe nanoribbons. Between -1 ~ +1 *V* bias voltage range, the *I-V* curves of zz-s and zz-u exhibit behaviors similar to a normal transistor, while the ac-s and ac-u show back-to-back p-n junction behavior. These results mean that the electronic transport performance of MoSSe nanoribbons strongly depends on their edge shapes, which is similarly with other 2D materials, such as graphene and MoS_2 [33, 35, 36]. Moreover, zigzag MoSSe nanoribbons have a stronger current than armchair nanoribbons over the whole voltage range. When the bias voltage is varied from 0 *V* to 1 *V*, the zz-s has the largest current in four nanoribbons ($I_{zz-s} > I_{zz-u} > I_{ac-s} > I_{ac-u}$). As shown in Figure 3d, the *dI/dV* curves of MoSSe nanoribbons are asymmetric, which is due to the atoms of MoSSe nanoribbons have shifted positions slightly after the structure was relaxed. Similar results were shown in prior research[33, 37].

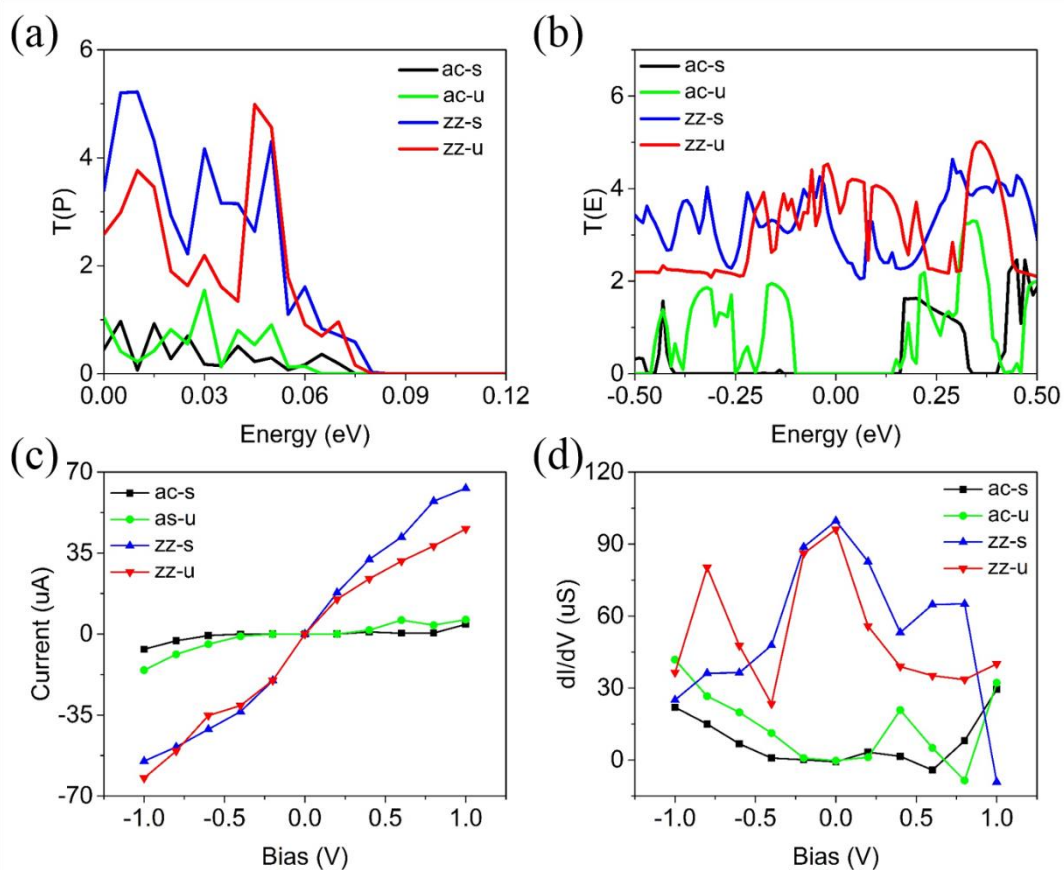*Figure 3. Electron transmission spectra (a), phonon transmission spectra (b), I-V (c) and dI/dV (d) curves of MoSSe nanoribbons.*

By integrating the calculated transmission spectra and rearranging equations (2), (4), (5) and (6), the electrical conductivity, thermal conductivity, Seebeck coefficient and *ZT* values of MoSSe nanoribbons can be readily obtained at 300 K. As shown in Figure 4, the chemical

potential (μ) indicated by the difference between the Fermi energy (E_F) and the DFT-predicted Fermi energy (E_F^{DFT}). For *p*-type doping chemical potential is negative while it is positive for *n*-type doping. In Figure 2, the band structures of ac-s, ac-u, zz-s and zz-u are different, which results in the peaks and valleys in the electrical conductivity curves. Figure 4a shows the electrical conductivity of zigzag MoSSe nanoribbons is higher than the armchair MoSSe nanoribbons, which is exactly matching with the results from the *I-V* and *dI/dV* curves. The developments of thermal conductivity of the ac-s, ac-u, zz-s and zz-u have a similar behavior as the electrical conductivity. Because of a metallic property of zigzag MoSSe nanoribbons, the heat transport performance of zigzag MoSSe nanoribbons is better than the armchair MoSSe nanoribbons. The Seebeck coefficients of ac-s, ac-u, zz-s and zz-u are shown in Figure 4c. In our band structures simulation (Figure 2), bandgap opening is shown in ac-s and ac-u, which results in a higher Seebeck coefficient maximum than those of zz-s and zz-u. In the ac-s, the maximum value is about 0.58 mV/K, which is slightly under the symmetric armchair MoS$_2$ nanoribbon ($\sim$0.70 mV/K)[27]. The *ZT* values of ac-s, ac-u, zz-s and zz-u as shown in the Figure 4d. It is clear that thermoelectric performance of armchair MoSSe nanoribbons is far superior than zigzag MoSSe nanoribbons. Two high *ZT* values at 300 K about 1.64 and 1.25 for the ac-s and ac-u respectively, which are around 150 times higher than those of zz-s and zz-u. In Figures 4a and b, the developments of electrical conductivities of ac-s, ac-u, zz-s and zz-u have similar trends with thermal conductivities, which illustrates that the high Seebeck coefficient induces a high *ZT* values in ac-s and ac-u.
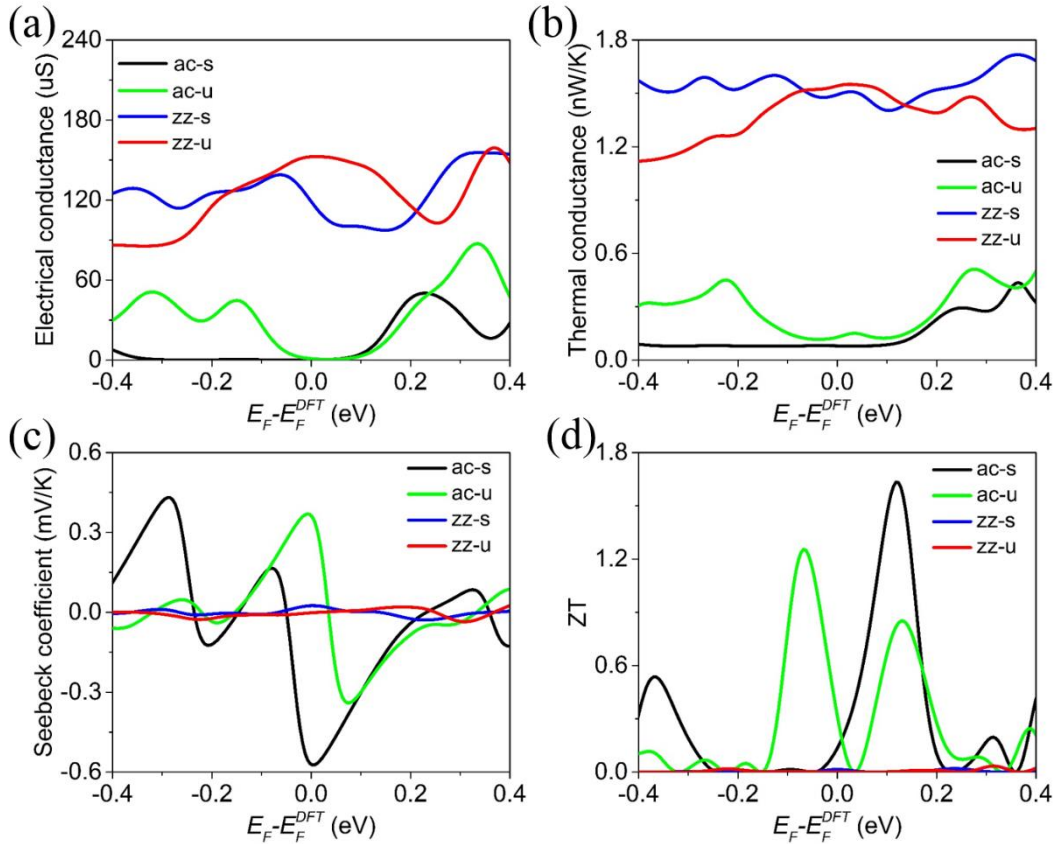

Figure 4. Electrical conductivity (a), thermal conductivity (b), Seebeck coefficient (c) and ZT values (d) of MoSSe nanoribbons.

As shown in Figure 5, we construct bilayer MoSSe (MoSSe-MoSSe) and graphene/MoSSe heterogenous. Bilayer MoSSe nanoribbons is constructed by attaching two monolayer MoSSe nanoribbons together with AA stacking type[38], while graphene/MoSSe heterogenous nanoribbons are constructed by attaching the monolayer MoSSe and graphene together with the Generalized Lattice Match (GLM) method[39]. Because the monolayer MoSSe has S atom and Se atom on each side, so we construct two stacking types with graphene, named as C/SMoSe and C/SeMoS. Due to the size of monolayer MoSSe and graphene cells are not commensurate, a 0.63% strain needs to build up at the graphene face to tune the lattice constant for matching with the MoSSe layer. In prior research, the mismatch strains of heterostructures are usually less than 3%[40-42], our 0.63% strain means an acceptable lattice mismatch between graphene and monolayer MoSSe. Figure 5a shows the fat band structure of the bilayer MoSSe. The red and blue lines mark the bands projection on the top and bottom layers of the bilayer MoSSe nanoribbon, respectively. Obviously, adding a layer on the monolayer MoSSe induces band-shift about 0.5 eV. In the bilayer MoSSe stack, the intrinsic electric field of individual layers induces a p-n junction across the systems[43]. As shown in Figures 5b and 5c, the purple and green lines represent the bands of MoSSe and graphene, respectively. The Dirac cone at the K point comes from the bands of the graphene layer. Moreover, the CBM and VBM of MoSSe layer shift from the K point (pristine monolayer MoSSe) to the Γ point, which is attributed to the band dispersion subjecting to the vdW interaction. Interestingly, the Dirac cone position of C/SMoSe stacking is on the Fermi level about 0.11 eV, which means the graphene layer has a carrier density of $8.95 \times 10^{11}/cm^2$ hole doping[44]. Because the monolayer MoSSe has an intrinsic dipole on the surface, inducing a 0.77 eV electrostatic potential difference from Se atom to S atom. In the C/SMoSe stacking, the electrons can be easily moved from Dirac cone to the valence band under the build-in electric field of MoSSe because the electron affinity of the monolayer MoSSe (3.71 eV) is close to the work function of the graphene (4.30 eV)[45]. However, in the C/SeMoS stacking, build-in electric field strength is not enough to support the electrons overcoming the bandgap of MoSSe (2.03 eV) and moving from the conduction band to the Dirac cone.
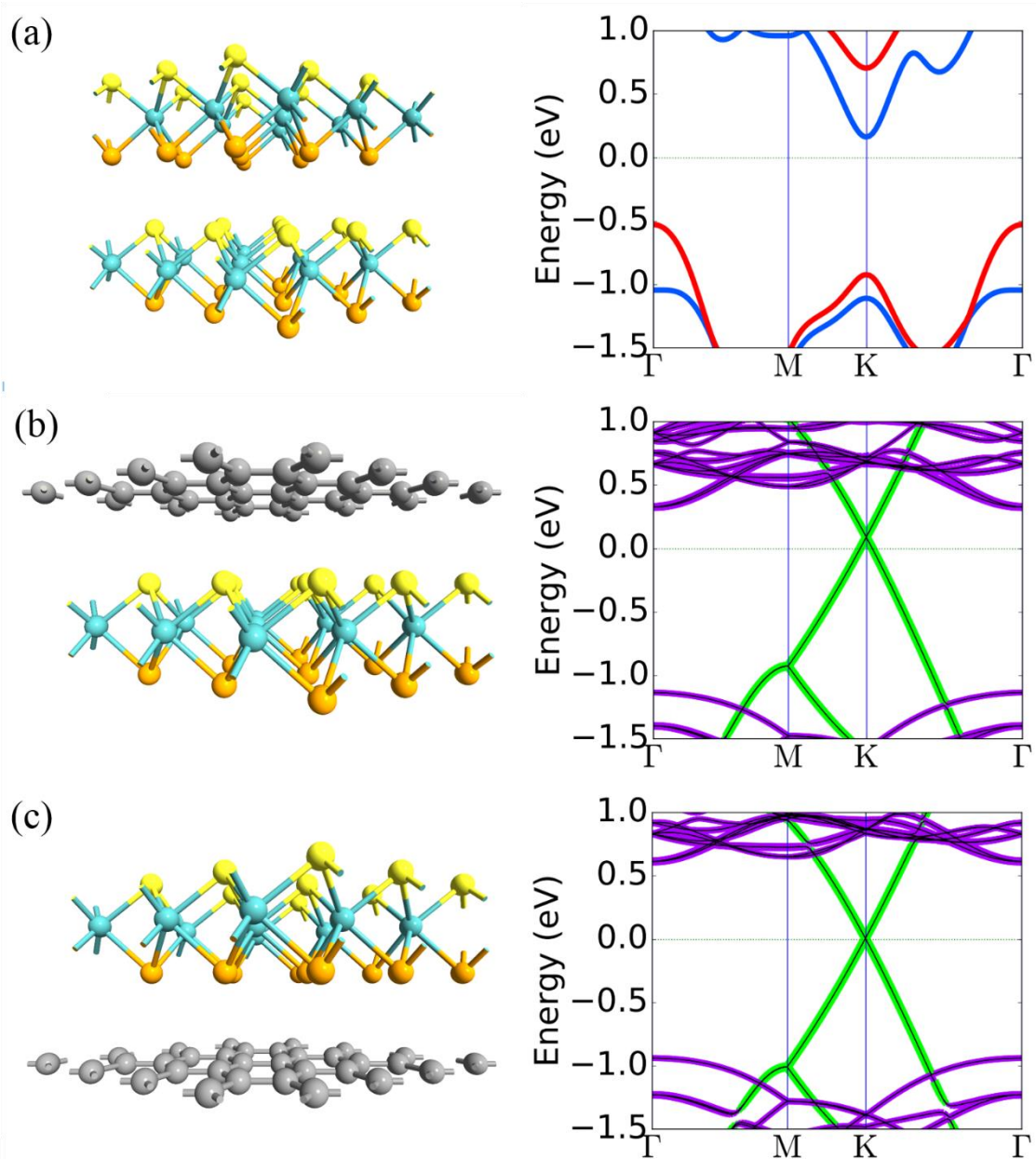
Figure 5. Relaxed structure and band structure of AA stacking bilayer MoSSe (a), C/SMoSe stacking graphene/MoSSe heterostructure (b) and C/SeMoS stacking graphene/MoSSe heterostructure (c).

Figure 6 plots the calculated 300 K electrical conductivity, thermal conductivity, Seebeck coefficient and *ZT* values as a function of chemical potential ($E_F - E_F^{DFT}$), which corresponds to the doping type of the system. We see from Figures 6a and 6b that the graphene/MoSSe heterostructure nanoribbons present much larger values compared with the bilayer MoSSe nanoribbon. Detailed examination of the band structures indicates that bilayer MoSSe nanoribbon has an opened bandgap of 0.71 eV, while the bandgap of graphene/MoSSe heterostructure nanoribbons are closed. As a result, we observe a much lower electrical conductivity in the bilayer MoSSe nanoribbon. Moreover, because graphene has a high thermal conductivity (4000 W/mK)[5], which induces a stronger heat transport capability in the

graphene/MoSSe heterostructure nanoribbons. We investigate bilayer MoSSe nanoribbon and vertical graphene/MoSSe heterostructure nanoribbons because the vdW interaction can limit the thermal conductivity in the normal direction to the 2D plane. In our paper, the thermal conductivity of bilayer MoSSe nanoribbon and vertical graphene/MoSSe heterostructure nanoribbons are only about 0.013 nW/K and 0.067 nW/K respectively, which are far lower than monolayer graphene (>4000 W/mK)[5] and MoSSe (345 W/K)[46]. We see from Figure 6c that the Seebeck coefficients of bilayer MoSSe nanoribbon and graphene/MoSSe heterostructure nanoribbons exhibit two clear peaks around the 0 eV. The absolute value is about 0.48 mV/K for bilayer MoSSe nanoribbon, which is larger than the graphene/MoSSe heterostructure nanoribbons (0.39 mV/K). Similar with electrical conductivity, the maximum of Seebeck coefficient also depends on the bandgap of three systems. Figure 6d shows the room temperature ZT values of bilayer MoSSe nanoribbon and graphene/MoSSe heterostructure nanoribbons. The ZT values of bilayer MoSSe nanoribbon, C/SMoSe stacking and C/SeMoS stacking heterostructure nanoribbons can be reached to 1.28, 1.16 and 2.01 by applying appropriate doping levels.
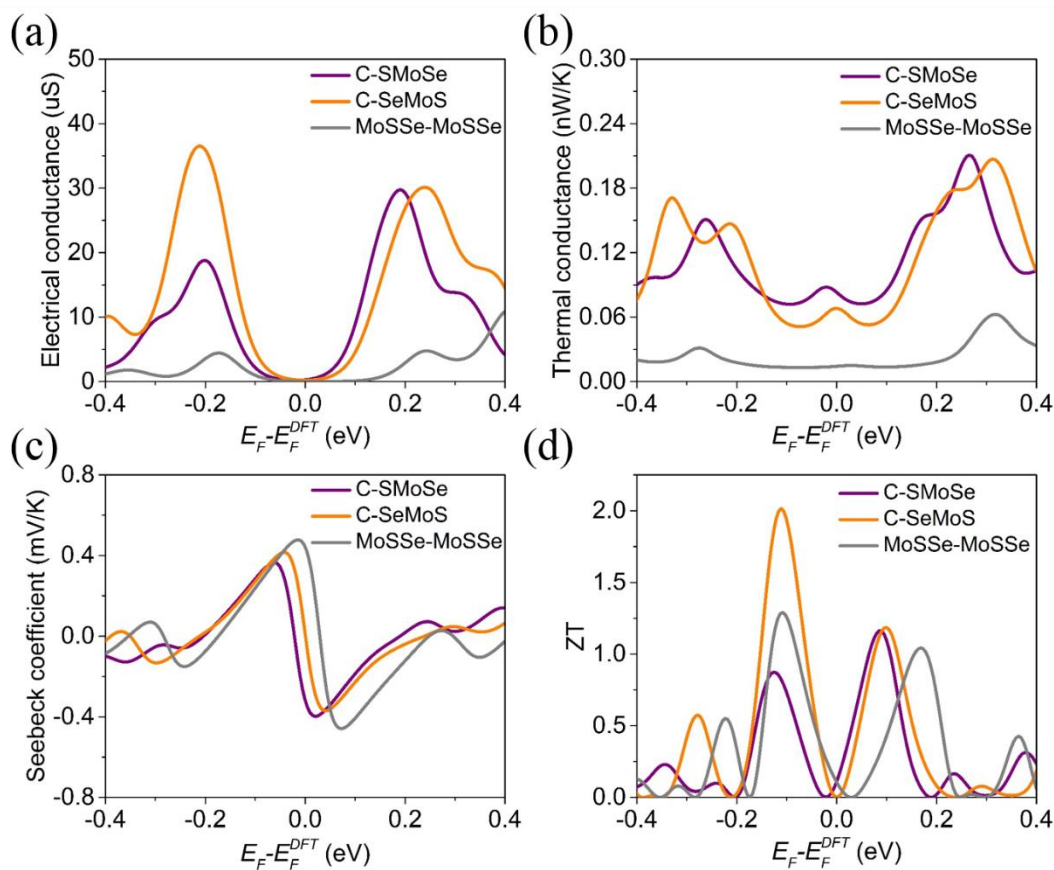

Figure 6. Electrical conductivity (a), thermal conductivity (b), Seebeck coefficient (c) and ZT values (d) of bilayer MoSSe nanoribbons and graphene/MoSSe heterostructure nanoribbons.

To evaluate the thermoelectric performance of MoSSe nanoribbons, we calculated the corresponding transport coefficients of $ZT > 1$ MoSSe nanoribbons in Table I. The Seebeck coefficients of five MoSSe nanoribbons at the ZT peak are very close, which means that the electrical conductivity and thermal conductivity are two key contributing parameters to lead to

a promising figure of merit for the MoSSe nanoribbons. Compared with the monolayer MoSSe nanoribbons (ac-s and ac-u), the electrical conductivity and thermal conductivity have much lower values in the bilayer MoSSe nanoribbons (C-S, C-Se and MoSSe-MoSSe), which indicates that vdW interaction between two layers limits the electrons and phonons transport in the normal direction to the 2D plane. Thermal conductivity calculation shows that phonon contribution to the thermal conductivity is much more than the electron contribution in the chemical potential range around the high ZT peaks. Our research suggests that symmetric armchair MoSSe and C/SeMoS stacked nanoribbons are better candidates for achieving better performance thermoelectric devices.

Table I. Calculated electronic and photonic transport coefficient of ZT>1 MoSSe nanoribbons at 300 K.

Structure	μ (eV)	S (mV/K)	Ge (μS)	κ_e (nW/K)	κ_p (nW/K)	ZT
ac-s	0.12	0.24	8.56	0.017	0.077	1.64
ac-u	-0.068	0.22	11.01	0.021	0.11	1.25
C-S	0.085	0.23	5.21	0.009	0.067	1.16
C-Se	-0.11	0.24	6.77	0.013	0.045	2.01
MoSSe-MoSSe	-0.11	0.21	1.36	0.0011	0.012	1.28

To investigate the effect of temperature on the thermoelectric performance of symmetric armchair MoSSe and C/SeMoS stacked nanoribbons, we calculated the variation of maximum values of ZT (Max ZT). As shown in Figure 7a, the Max ZT of C/SeMoS stacking nanoribbons increases to the maximum when T < 350 K, while the Max ZT reduces at high temperatures (T>350 K). However, in the Figure 7b, the Max ZT of the symmetric armchair MoSSe nanoribbon monotonic increases with the increase of temperature until 550 K. The highest ZT values of symmetric armchair MoSSe and C/SeMoS stacked nanoribbons can approach 2.01 and 2.31 at 550 K and 350 K, respectively. To explain the reason of different ZT-temperature relations in above two structures, we calculated k_p, Ge, S^2Ge and S^2GeT shown in Figures 7c - 7f. Obviously, the electrical conductivity and phonon contribution to the thermal conductivity increase with the rise of temperature, then tend to be stable at high temperature. Moreover, the electrical conductivity and phonon thermal conductivity of the C/SeMoS stacking nanoribbon are weaker than the symmetric armchair MoSSe nanoribbon from 50 K to 550 K because the vdW interaction hinders the electron and phonon transport between two layers. In the C/SeMoS stacking nanoribbon (Figure 7e), the extreme point of S^2Ge curve appears at 300 K, while shifts to 450 K in the S^2GeT curve, which means the transition of the Max ZT at 350 K (Figure 7a) is induced by the variation of the phonon thermal conductivity. In the symmetric armchair MoSSe nanoribbon (Figure 7f), although the extreme point of S^2Ge curve appears at the 300 K, while the relation of S^2GeT with temperature is nearly linear. Therefore, the Max ZT of this type monotonically increases with the increase of temperature. These results indicate that phonon thermal conductivity and temperature are key factors in the variation of MAX ZT values.
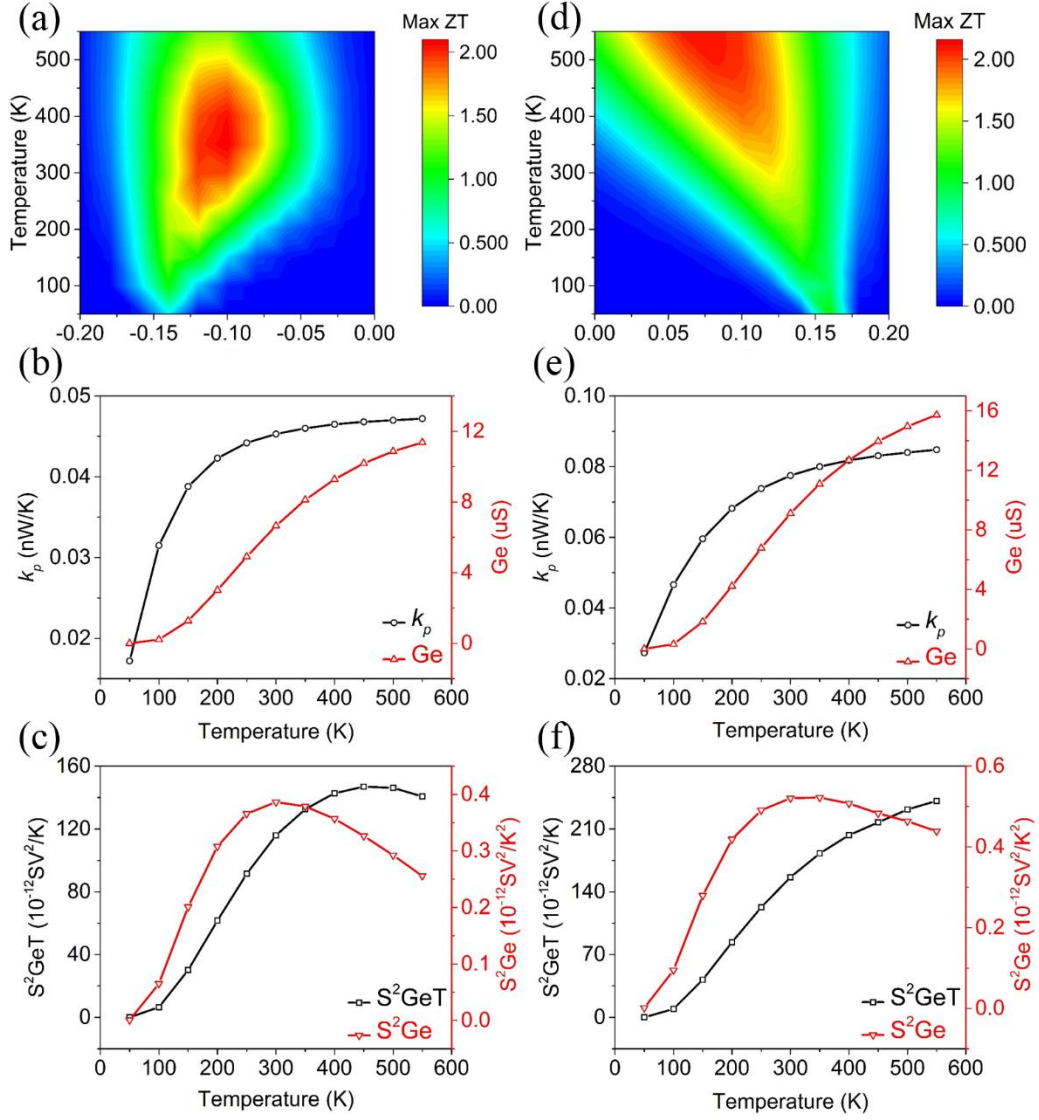
Figure 7. Max ZT, k_p, Ge, S^2Ge and S^2GeT of symmetric armchair MoSSe nanoribbon (a)-(c) and C/SeMoS stacking graphene/MoSSe heterostructure nanoribbon (d)-(f).

A good thermoelectric device should have an optimized trade-off between the electrical conductivity, thermal conductivity and Seebeck coefficient. Although graphene has a high electrical conductivity, the thermoelectric figure of merit was unsatisfactory because of its high thermal conductivity (>4000 W/mK) and small Seebeck coefficient (<100 µV/K)[5]. For monolayer MoS_2, it has a large theoretical thermoelectric power factor with 28 mW/mK^2 at 300 K[26]. Based on this thermoelectric power factor and experimentally obtained lattice thermal conductivity (34.5±4 W/mK), a *ZT* value of 0.5 is reported at 300 K[47]. With the same width as our MoSSe nanoribbon, the theoretical results showed that *ZT* values of MoS_2 nanoribbons were only 1.3 and 0.8 for *n* type and *p* type doping, respectively[27]. In previous theoretical research, a high *ZT* value about 7.4 can be obtained in the MoS_2/$MoSe_2$ nanoribbons, while the temperature around 800 K[30]. The latest research indicates that lattice thermal conductivity in MoSSe monolayer is 345 W/K at room temperature, which is much lower than the MoS_2 monolayer[46]. In our manuscript, the Seebeck coefficient of graphene/SeMoS stacked layers and

symmetric armchair MoSSe nanoribbons is calculated to be 0.24 mV/K, which is nearly 2.4 times higher than the pristine graphene. Moreover, a strong reduction of thermal conductivity for graphene/SeMoS stacked layers (0.058 nW/K) compared with the monolayer graphene and MoS_2 has been demonstrated, which is due to that the van der Waals interaction limits the thermal conductivity in the normal direction to the 2D plane. The *ZT* values of 2.01 and 1.64 can be achieved for graphene/SeMoS stacked layers and symmetric armchair MoSSe nanoribbons at 300 K, which demonstrates better thermoelectric performances than graphene, MoS_2 monolayer, MoS_2 nanoribbon, and MoSSe monolayer. Hence, the symmetric armchair MoSSe and C/SeMoS stacked nanoribbons are better candidates in thermoelectric devices.

Conclusions:

In this work, for the first time, the electron, phonon transport and thermoelectric performance of monolayer MoSSe nanoribbons, bilayer MoSSe nanoribbons and graphene/MoSSe heterogeneous nanoribbons are systematically researched using the first-principle methods with non-equilibrium Green's function. It is discovered that *ZT* values of 2.01 and 1.64 can be achieved for graphene/SeMoS stacked layers and symmetric armchair MoSSe nanoribbons at 300 K respectively. It is found that the Max *ZT* values of C/SeMoS stacked nanoribbons increase to the maximum when T<350 K and display a decreasing trend at high temperature (T>350 K). However, the Max *ZT* values of symmetric armchair MoSSe nanoribbons monotonically increase with increasing temperature up to 550 K. Results indicate that phonon thermal conductivity and temperature are key factors in the variation of Max *ZT* values in MoSSe nanoribbons. The present study paves the way for future design and implementation of high-performance thermoelectric devices.

Acknowledgements:

References:

1. Y. Chen, T. Jayasekera, A. Calzolari, K. W. Kim and M. B. Nardelli, *J. Phys-Condens. Mat.*, 2010, **22**.

2. G. J. Snyder and E. S. Toberer, *Nat. Mater.*, 2008, **7**, 105-114.

3. D. Tainoff, A. Proudhom, C. Tur, T. Crozes, S. Dufresnes, S. Dumont, D. Bourgault and O. Bourgeois, *Nano Energy*, 2019, **57**, 804-810.

4. M. Haras and T. Skotnicki, *Nano Energy*, 2018, **54**, 461-476.

5. P. Dollfus, V. H. Nguyen and J. Saint-Martin, *J. Phys-Condens. Mat.*, 2015, **27**.

6. X. Cui, G. H. Lee, Y. D. Kim, G. Arefe, P. Y. Huang, C. H. Lee, D. A. Chenet, X. Zhang, L. Wang, F. Ye, F. Pizzocchero, B. S. Jessen, K. Watanabe, T. Taniguchi, D. A. Muller, T. Low, P. Kim and J. Hone, *Nat. Nanotechnol.*, 2015, **10**, 534-540.

7. M. Buscema, M. Barkelid, V. Zwiller, H. S. J. van der Zant, G. A. Steele and A. Castellanos-Gomez, *Nano Lett.*, 2013, **13**, 358-363.

8. A. Taube, J. Judek, A. Lapiriska and M. Zdrojek, *Acs Appl Mater Inter*, 2015, **7**, 5061-5065.

9. G. Zhang and Y. W. Zhang, *J. Mater. Chem. C*, 2017, **5**, 7684-7698.

10. Q. Q. Wu, H. Sadeghi and C. J. Lambert, *Nanoscale*, 2018, **10**, 7575-7580.

11. A. Aiyiti, S. Q. Hu, C. R. Wang, Q. Xi, Z. F. Cheng, M. G. Xia, Y. L. Ma, J. B. Wu, J. Guo, Q. L. Wang, J. Zhou, J. Chen, X. F. Xu and B. W. Li, *Nanoscale*, 2018, **10**, 2727-2734.

12. A. Sajedi-Moghaddam, E. Saievar-Iranizad and M. Pumera, *Nanoscale*, 2017, **9**, 8052-8065.

13. A. Y. Lu, H. Y. Zhu, J. Xiao, C. P. Chuu, Y. M. Han, M. H. Chiu, C. C. Cheng, C. W. Yang, K. H. Wei, Y. M. Yang, Y. Wang, D. Sokaras, D. Nordlund, P. D. Yang, D. A. Muller, M. Y. Chou, X. Zhang and L. J. Li, *Nat. Nanotechnol.*, 2017, **12**, 744-+.

14. J. Zhang, S. Jia, I. Kholmanov, L. Dong, D. Q. Er, W. B. Chen, H. Guo, Z. H. Jin, V. B. Shenoy, L. Shi and J. Lou, *ACS Nano*, 2017, **11**, 8192-8198.

15. S. Deng, L. J. Li and P. Rees, *ACS Appl. Nano Mater.*, 2019, **2**, 3977-3988.

16. L. Dong, J. Lou and V. B. Shenoy, *ACS Nano*, 2017, **11**, 8242-8248.

17. M. Palsgaard, T. Gunst, T. Markussen, K. S. Thygesen and M. Brandbyge, *Nano Lett.*, 2018, **18**, 7275-7281.

18. W. J. Yin, B. Wen, G. Z. Nie, X. L. Wei and L. M. Liu, *J. Mater. Chem. C*, 2018, **6**, 1693-1700.

19. X. C. Ma, X. Wu, H. D. Wang and Y. C. Wang, *J Mater Chem A*, 2018, **6**, 2295-2301.

20. Y. J. Ji, M. Y. Yang, H. P. Lin, T. J. Hou, L. Wang, Y. Y. Li and S. T. Lee, *J. Phys. Chem. C*, 2018, **122**, 3123-3129.

21. Z. Y. Guan, S. Ni and S. L. Hu, *J. Phys. Chem. C*, 2018, **122**, 6209-6216.

22. F. P. Li, W. Wei, P. Zhao, B. B. Huang and Y. Dai, *J. Phys. Chem. Lett.*, 2017, **8**, 5959-5965.

23. Y. Liang, J. W. Li, H. Jin, B. B. Huang and Y. Dai, *J. Phys. Chem. Lett.*, 2018, **9**, 2797-2802.

24. Y. N. Wen, M. G. Xia and S. L. Zhang, *Comp Mater Sci*, 2018, **152**, 20-27.

25. C. J. Shih, Q. H. Wang, Y. Son, Z. Jin, D. Blankschtein and M. S. Strano, *ACS Nano*, 2014, **8**, 5790-5798.

26. H. Babaei, J. M. Khodadadi and S. Sinha, *Appl. Phys. Lett.*, 2014, **105**.

27. D. D. Fan, H. J. Liu, L. Cheng, P. H. Jiang, J. Shi and X. F. Tang, *Appl. Phys. Lett.*, 2014, **105**.

28. W. Huang, X. Luo, C. K. Gan, S. Y. Quek and G. C. Liang, *Phys. Chem. Chem. Phys.*, 2014, **16**, 10866-10874.

29. K. X. Chen, X. M. Wang, D. C. Mo and S. S. Lyu, *J. Phys. Chem. C*, 2015, **119**, 26706-26711.

30. Y. L. Ouyang, Y. E. Xie, Z. W. Zhang, Q. Peng and Y. P. Chen, *J. Appl. Phys.*, 2016, **120**.

31. Atomistix ToolKit (ATK), https://quantumwise.com/. .

32. S. Grimme, *J. Comput. Chem.*, 2006, **27**, 1787-1799.

33. H. Pan and Y. W. Zhang, *Journal of Materials Chemistry*, 2012, **22**, 7280-7290.

34. S. Zhang, H. Jin, C. Long, T. Wang, R. Peng, B. B. Huang and Y. Dai, *J Mater Chem A*, 2019, **7**, 7885-7890.

35. H. Zheng, H. J. Liu, X. J. Tan, H. Y. Lv, L. Pan, J. Shi and X. F. Tang, *Appl. Phys. Lett.*, 2012, **100**.

36. S. Deng, C. Xiang, Y. Zhang and L. J. Li, *Carbon*, 2019, **145**, 622-628.

37. T. H. Liu, Y. C. Chen, C. W. Pao and C. C. Chang, *Appl. Phys. Lett.*, 2014, **104**.

38. K. Kosmider and J. Fernandez-Rossier, *Phys. Rev. B*, 2013, **87**.

39. L. Jelver, P. M. Larsen, D. Stradi, K. Stokbro and K. W. Jacobsen, *Phys. Rev. B*, 2017, **96**.

40. Z. L. Wang, Q. Chen and J. L. Wang, *J. Phys. Chem. C*, 2015, **119**, 4752-4758.

41. Y. Matsushita, H. Nishi, J. Iwata, T. Kosugi and A. Oshiyama, *Phy Rev Mater*, 2018, **2**, 010801.

42. S. Deng, Y. Zhang and L. J. Li, *Appl. Surf. Sci.*, 2019, **476**, 308-316.

43. C. Long, Y. Dai, Z. R. Gong and H. Jin, *Phys. Rev. B*, 2019, **99**.

44. W. Hu, Z. Y. Li and J. L. Yang, *J. Chem. Phys.*, 2013, **138**, 124706.

45. Y. J. Yu, Y. Zhao, S. Ryu, L. E. Brus, K. S. Kim and P. Kim, *Nano Lett.*, 2009, **9**, 3430-3434.

46. S. D. Guo, *Phys. Chem. Chem. Phys.*, 2018, **20**, 7236-7242.

47. R. S. Yan, J. R. Simpson, S. Bertolazzi, J. Brivio, M. Watson, X. F. Wu, A. Kis, T. F. Luo, A. R. H. Walker and H. G. Xing, *ACS Nano*, 2014, **8**, 986-993.

Enhanced thermoelectric performance of monolayer MoSSe, bilayer

MoSSe and graphene/MoSSe heterostructure nanoribbons

Shuo Deng[†‡] Lijie Li[*‡], Owen J. Guy[*‡], and Yan Zhang[*§]

[†]Wuhan University of Technology, Wuhan 430070, China

[‡]College of Engineering, Swansea University, Swansea SA1 8EN, UK

[§]School of Physics, University of Electronic Science and Technology of China, Chengdu, China.

[*]Emails: L.Li@swansea.ac.uk; o.j.guy@swansea.ac.uk; zhangyan@uestc.edu.cn